



**HAL**  
open science

## Assessing craniofacial growth and form without landmarks: A new automatic approach based on spectral methods

Robin Magnet, Kevin Bloch, Maxime Taverne, Simone Melzi, Maya Geoffroy, Roman H Khonsari, Maks Ovsjanikov

### ► To cite this version:

Robin Magnet, Kevin Bloch, Maxime Taverne, Simone Melzi, Maya Geoffroy, et al.. Assessing craniofacial growth and form without landmarks: A new automatic approach based on spectral methods. *Journal of Morphology*, 2023, 284 (8), pp.e21609. 10.1002/jmor.21609 . hal-04352348

**HAL Id: hal-04352348**

**<https://hal.science/hal-04352348>**

Submitted on 21 Dec 2023

**HAL** is a multi-disciplinary open access archive for the deposit and dissemination of scientific research documents, whether they are published or not. The documents may come from teaching and research institutions in France or abroad, or from public or private research centers.

L'archive ouverte pluridisciplinaire **HAL**, est destinée au dépôt et à la diffusion de documents scientifiques de niveau recherche, publiés ou non, émanant des établissements d'enseignement et de recherche français ou étrangers, des laboratoires publics ou privés.

# Assessing craniofacial growth and form without landmarks: A new automatic approach based on spectral methods

Robin Magnet<sup>1</sup>  | Kevin Bloch<sup>2</sup> | Maxime Taverne<sup>2</sup>  | Simone Melzi<sup>3</sup> | Maya Geoffroy<sup>2</sup> | Roman H. Khonsari<sup>2</sup>  | Maks Ovsjanikov<sup>1</sup> 

<sup>1</sup>LIX, École Polytechnique, IP Paris, Palaiseau, France

<sup>2</sup>Laboratoire "Forme et Croissance du Crâne", Hôpital Necker-Enfants Malades, Assistance Publique Hôpitaux de Paris, Faculté de Médecine, Université Paris Cité, Paris, France

<sup>3</sup>Department of Informatics, Systems and Communication, University of Milano-Bicocca, Milan, Italy

## Correspondence

Robin Magnet, LIX, École Polytechnique, IP Paris, Palaiseau, France.  
Email: [rmagnet@lix.polytechnique.fr](mailto:rmagnet@lix.polytechnique.fr)

## Funding information

European Research Council; Agence Nationale de la Recherche

## Abstract

We present a novel method for the morphometric analysis of series of 3D shapes, and demonstrate its relevance for the detection and quantification of two craniofacial anomalies: trigonocephaly and metopic ridges, using CT-scans of young children. Our approach is fully automatic, and does not rely on manual landmark placement and annotations. Our approach furthermore allows to differentiate shape classes, enabling successful differential diagnosis between trigonocephaly and metopic ridges, two related conditions characterized by triangular foreheads. These results were obtained using recent developments in automatic nonrigid 3D shape correspondence methods and specifically spectral approaches based on the functional map framework. Our method can capture local changes in geometric structure, in contrast to methods based, for instance, on global shape descriptors. As such, our approach allows to perform automatic shape classification and provides visual feedback on shape regions associated with different classes of deformations. The flexibility and generality of our approach paves the way for the application of spectral methods in quantitative medicine.

## KEYWORDS

craniofacial malformation, diagnostic tool, functional maps, landmark-free morphometrics, metopic ridge, morphometrics, skull malformation, spectral analysis, trigonocephaly

## 1 | INTRODUCTION

Trigonocephaly is a puzzling congenital craniofacial malformation secondary to a premature fusion of the metopic suture, located between the two frontal bones. Trigonocephaly is characterized by a triangular, keel-shaped forehead, biparietal widening, and hypotelorism (Kolar & Salter, 1997). Interestingly, the usual theories on craniofacial growth are of little help to understand the mechanisms leading to this malformation, and there is currently no clear explanation accounting for the striking increase in its prevalence in the last three decades (van der Meulen et al. 2009). Trigonocephaly requires surgical correction before 1 year of age for esthetic and

functional imperatives. In this context, early and reliable diagnosis is key in the management of trigonocephaly (Mathijssen & Working Group Guideline Craniosynostosis, 2021).

Numerous anthropometric measurements have been proposed in the literature to help diagnose this condition (Calandrelli et al., 2020; Kellogg et al., 2012), and also to differentiate trigonocephaly from metopic ridges, a minor anomaly due to an excessive ossification of the metopic suture, without orbital deformation or biparietal widening, that does not generally require surgical correction. Quantifying morphological differences between trigonocephaly and metopic ridges can be hard to perform reliably. Instead, distinguishing between these two conditions is typically performed using purely

subjective, qualitative analysis. Furthermore, even though the differences between these two conditions are three-dimensional, most of the metrics proposed in the literature to differentiate them are twodimensional (Birgfeld et al., 2019, 2013), and few are three-dimensional (Cho et al., 2016).

The quantification of three-dimensional shapes requires the use of specific statistical approaches such as geometric morphometrics (Bookstein, 1997; Gunz & Mitteroecker, 2013; Klingenberg, 2002). These approaches are now commonly used in biomedical sciences, to better describe phenotypes, study growth, and evaluate treatment outcomes (Rutland et al., 2021). Usual morphometric approaches rely on the placement of landmarks, and subsequent analysis of their variability using rigid and nonrigid registration (Adams et al., 2004; Bookstein, 1982, 1997, 2019; Klingenberg, 2016; Slice, 2007; Webster & Sheets, 2010). This procedure presents many indisputable advantages including the preservation of homology of anatomical regions throughout data sets encompassing great interspecific variation (Gillet et al., 2019; Mallet et al., 2019; Palci & Lee, 2019), or along different developmental stages (Fabre et al., 2020; O'Higgins & Jones, 1998; Watanabe & Slice, 2014). Although intraoperator biases related to the manual placement of reference points exist, they have been extensively studied (Arnqvist & Mårtensson, 1998; von Cramon-Taubadel et al., 2007; Daboul et al., 2018; Wärmländer et al., 2019), allowing for their detailed quantification. However, interoperator biases are still more difficult to assess, and this could be important in the era of big data. Also, classical geometric morphometrics may face some other limitation like missing data and/or topological discrepancies. Several attempts of applying landmark-free approaches to shape assessment have been recently proposed in the literature (Biasotti et al., 2016; Sahillioglu, 2020; Toussaint et al., 2021). Among all 3D shape assessment methods with or without landmarks, spectral techniques (Ovsjanikov et al., 2012, 2017), originally developed for computer graphics, have rarely been applied to the medical field to date.

Unlike standard geometric approaches, spectral shape analysis goes beyond the 3D geometry of a surface and analyzes *functions* defined on the shapes, which comes with a rich and flexible mathematical framework. In particular, functional maps (Ovsjanikov et al., 2012) and their numerous extensions (Huang et al., 2020; Melzi et al., 2019) allow to compute highly accurate dense point-to-point correspondences, and can be adapted to a wide range of settings and deformation models (Ren et al., 2021).

Notable previous works (Kitchell et al., 2018; Klein et al., 2017; Niethammer et al., 2007; Nitzken et al., 2014; Shishegar et al., 2021) have used partly outdated spectral methods for medical data analysis, and especially the so-called shape DNA descriptors (Reuter et al., 2009). These methods typically relied on restricted deformation models such as near-isometries, and, importantly, only enabled *global* shape comparison, by associating a single descriptor vector to each shape. Unfortunately, as we demonstrate below, this is insufficient to reliably distinguish subtle differences that might exist across different shape categories.

In contrast, functional maps provide a general and flexible framework that has proven capable of efficiently obtaining accurate

fully-automatic *landmark-free local* correspondences between shapes, leading to state-of-the-art results even in challenging settings like partiality (Attaiki et al., 2021; Rodolà et al., 2017) or non-isometry (Dyke et al., 2020; Ren et al., 2018). Unlike global shape embeddings, local correspondences enable more accurate analysis of shape collections, highlighting precise *regions* associated with shape changes, and even building task-specific deformation models. Furthermore, spectral methods can be used to refine noisy initial correspondences obtained through rigid alignment, as we demonstrate in this paper.

In this work we leveraged these recent state-of-the-art fully automatic shape correspondence methods, which we adapted to fit within a morphometric analysis pipeline to study morphological differences between trigonocephaly, metopic ridges, and controls. Our results pave the way for the use of this new set of methods in quantitative medicine.

## 2 | MATERIALS AND METHODS

### 2.1 | Overview

We used a template-based morphometric analysis framework, where deformations between the template and each shape were defined using dense vertex-to-vertex correspondences—that is assigning a point on the target shape for each point on the template. Both the correspondences and the template were obtained automatically using a landmarks-free approach by adapting recent developments in the functional map framework (Huang et al., 2020; Melzi et al., 2019). The proposed pipeline is fast, fully automatic, flexible as it can handle different types of deformations, and provides visual feedback on zones undergoing the most important shape modifications.

Our work, briefly described on Algorithm 1, builds on a variety of recent works (Huang et al., 2019, 2020), for which we here only provide a detailed description of the necessary modifications. We refer the interested reader to the original publications for a complete description of the methods. A complete implementation of our approach, that can be used by other researchers is available at [https://github.com/RobinMagnet/Morpho\\_FMaps](https://github.com/RobinMagnet/Morpho_FMaps).

### 2.2 | Data

This study relies on the reuse of retrospective data acquired during standard patient care and complies to MR-004 (CNIL1818709X, 2018-155, #110, 03.05.2018). All patients were informed of the reuse of their personal data for this specific study. Our data set included all patients with non-syndromic trigonocephaly that benefited from fronto-orbital advancement at Necker—Enfants Malades Hospital (Assistance Publique-Hôpitaux de Paris), at the National Reference Center for Craniosynostoses and Craniofacial Malformations (CRMR CRANIOST; Filière Maladies Rares TeteCou) from 2004 to 2019 with an available digital preoperative CT-scan. In

addition, all patients diagnosed with metopic ridges managed in the same center during the same period, with an available digital CT-scan, were also included. For metopic ridges, all scans were performed for diagnostic purposes before patients were sent to our center, radiological examination being of little use in this condition in the vast majority of cases. This cohort of patients with metopic ridges thus corresponded to a specific subset of patients that raised diagnostic questions with trigonocephaly, and was interesting in the context of the assessment of a classification method. The final differential diagnosis between trigonocephaly and metopic ridges was based on the expert opinion of the craniofacial surgeons of the National Reference Center. Control age-matched patients were included, with available digital CT-scans performed in the emergency department of the same hospital (for acute headache, soft-tissue infections, epilepsy, or trauma). All control CT-scans were assessed by two independent reviewers (craniofacial surgeon and pediatric radiologist), to ensure that only scans without skull fractures, craniofacial anomalies, structural abnormalities, and of sufficient quality for 3D reconstruction were included. Age and gender were noted for all patients. The data set consisted in  $N = 155$  CT-scans of skulls including  $n_t = 85$  patients with trigonocephaly (mean age:  $219.3 \pm 81.4$  days),  $n_m = 27$  patients with a metopic ridge (mean age:  $379.25 \pm 224.7$  days), and  $n_c = 43$  control patients (mean age:  $218.7 \pm 107.8$  days). The detailed age distribution for each group is provided in the supplementary material. The scans were segmented using 3D Slicer (Fedorov et al., 2012), and skulls were exported as 3D surface objects. The surface objects generated from segmentation masks consisted in watertight meshes composed of an inner and an outer surface (Figure 1). Due to the segmentation process which forced watertightness, scan quality, and variation in ossification across patients, several skulls presented multiple either natural or

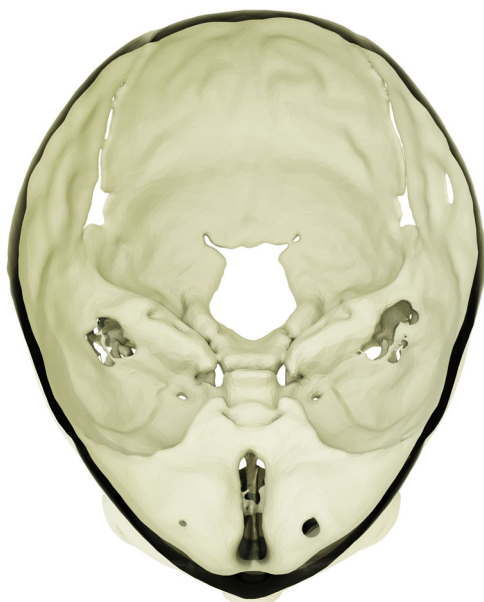


**FIGURE 1** Visualization of the inner and outer surfaces of a mesh in horizontal section.

artificial surface interruptions (especially around the orbital cavity and on the anterior skull base) connecting the two layers of the surface at unusual places. This generated both severe topological dissimilarities between the surfaces due to the addition of several holes, and highly nonisometric transformations that distorted geodesic distances between inner and outer surfaces (Figure 2). While addressing these changes can pose challenges for certain shape analysis approaches, using the functional map framework proved effective in mitigating this issue. In particular, while Section 2.4 showed a small adaptation to double-surface for initialization, we did not adapt the method to avoid or explicitly handle topological challenges present in the data.

Each scan in the collection was remeshed to reach roughly 40,000 triangles, then normalized and centered, and isolated components were automatically removed. The eigenfunctions of the Laplace–Beltrami operator, introduced in Section 2.3, were precomputed separately for each shape.

### 2.3 | Functional maps

We based our approach on the Consistent ZoomOut algorithm (Huang et al., 2020), a landmark-free method, which allows to refine noisy initial correspondences in a collection of shapes using functional maps.

Functional maps were introduced by Ovsjanikov et al. (2012) as an efficient and adjustable way to perform shape correspondence. While standard shape matching methods directly optimized for pointwise correspondences between two surfaces, functional maps considered instead transferring *real-valued functions* across shape pairs (Figure 3).

More precisely, the key idea of functional maps consisted in encoding functions using a basis on each shape and then representing correspondences as linear operators across basis functions of different shapes. These linear operators could be encoded as compact matrices (functional maps), that intuitively allowed to “translate” across different bases. Crucially the size of these functional maps was independent of the number of vertices on each shape, and only depended on the chosen basis size. In practice, the standard choice was to use the eigenfunctions of the Laplace–Beltrami operator as the functional basis on each shape (Figure 4), as they presented a natural generalization of Fourier analysis to general domains. In practice, this meant that the standard functional maps pipeline (Ovsjanikov et al., 2017) consisted in first computing  $K \approx 50$ – $100$  basis functions on each shape, optimizing for a  $K \times K$  functional map matrix, and then converting this matrix to a dense point-to-point correspondence. As greater values of  $K$  corresponded to more precise point-wise maps, most recent algorithms (Huang et al., 2020; Melzi et al., 2019; Ren et al., 2021) iteratively refined an initial small-sized (blurry) functional map into a bigger one.

Functional maps have also been used to establish correspondences within *shape collections* (Huang et al., 2020), which can lead to

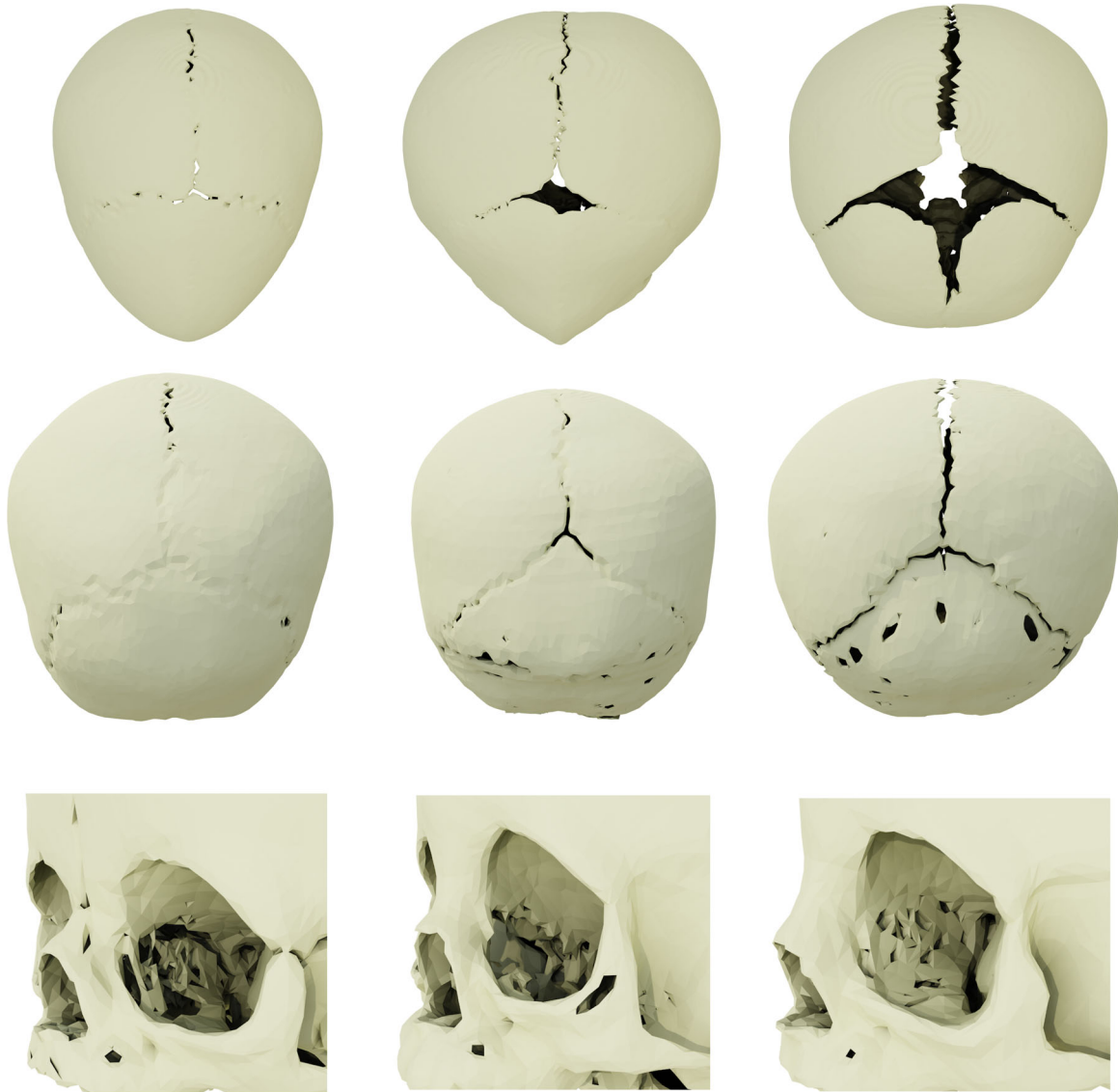


**FIGURE 2** The data set included highly nonisometric deformations (top and middle row) as well as topological dissimilarities around the orbital cavity (bottom row).

more accurate results, by exploiting collection-wise consistency constraints. In particular, functional map networks (FMN) consider collections of shapes  $(\mathcal{S}_i)_{i=1}^N$ , related to each other with functional correspondences, encoded as  $K \times K$  matrices, which together define a *graph* of correspondences (Huang et al., 2019, 2020; Nguyen et al., 2011). Using an initial FMN, the Consistent ZoomOut algorithm (Huang et al., 2020) allows to establish *consistent* maps across any shape pair, by constructing a virtual template referred to as a “limit shape.” The limit shape is a purely algebraic construct (intuitively it corresponds to a space where functions from all shapes get averaged out) and does not have a concrete geometric structure. However, Consistent ZoomOut allows to build functional maps between this limit shape and every shape in the collection, leading to accurate correspondences between arbitrary shape pairs, even those not present in the original FMN.

## 2.4 | Computing correspondences

Consistent ZoomOut (Huang et al., 2020) requires initial correspondences to build the network. These initial correspondences can be very approximate as they are later refined by the algorithm. In this work, we relied on a rigid alignment of the surfaces, which was made possible as all skulls were roughly facing the same direction due to the acquisition process. Note that our method tolerated noisy initial maps and no manually placed anatomical landmarks were required.

Specifically, initial maps between a pair of shapes  $S_1$  and  $S_2$  were computed as follows. We first applied an iterative closest point (ICP) algorithm (Besl & McKay, 1992) for approximate rigid alignment. Using this initialization, each vertex  $y \in S_2$  was then associated to the nearest vertex  $x = T(y) \in S_1$  with a coherent normal, that is,

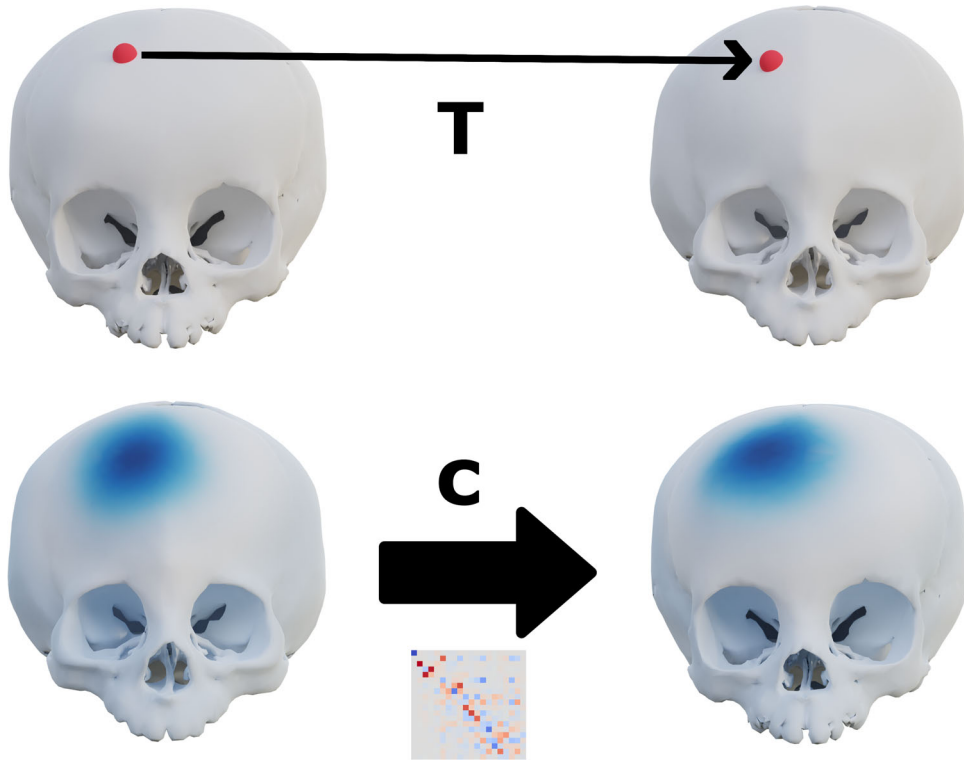


**FIGURE 3** Comparison of point-based and functional correspondences. Top: A point on one shape was transferred to another shape using a vertex-to-vertex map  $T$ . Bottom: A function was transferred using a functional map  $C$ . The image below the arrow is a representation of the entries of the functional map matrix. Note that these two transfers do not require  $T$  or  $C$  to be ground truth maps.

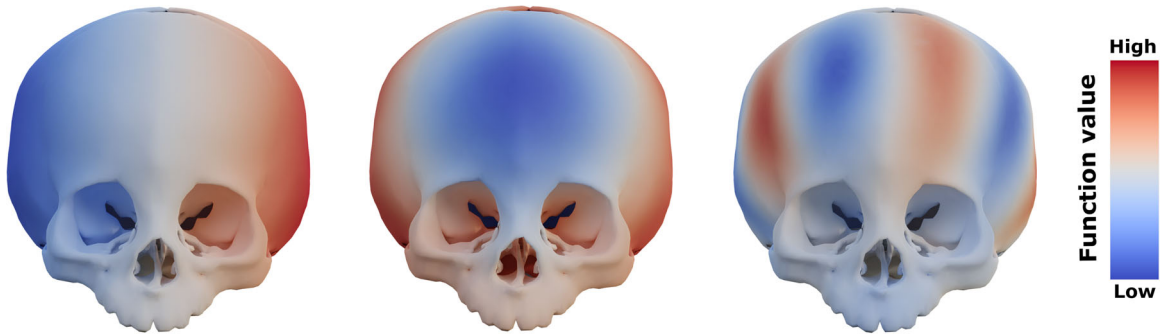


**FIGURE 4** Examples of low frequency (i.e., slowly varying) eigenfunctions of the Laplace-Beltrami operator.

$y \mapsto x = \underset{x_i \in S_1, (n_{x_i}, n_y) > 0}{\operatorname{argmin}} \|x_i - y\|^2$ . This procedure ensured that even if the alignment was not clinically relevant, the inner and outer surfaces (described in Section 2.2) were differentiated as schematically explained in Figure 5. In Figure 5, without normal consistency, point  $x_1$ , which lied on the outer surface of  $S_1$ , was mapped to point  $y_2$  on the inner surface of  $S_2$ , and  $x_2$  was also mapped to  $y_2$ . The obtained correspondences  $T$  could then be transformed into a functional map  $C$  of size  $K \times K$ . Note that these initial maps were of poor quality as they relied on an ICP alignment, which may have poorly aligned clinically relevant areas of the skull. Furthermore, the normal consistency procedure could have failed in zones with high curvature. We thus refined them using Consistent ZoomOut before performing downstream analysis tasks.

We have significantly improved the speed of both the initialization and refinement steps by using only small subset of 2000 randomly chosen pairs out of the approximately 12,000 possibilities. The initial functional correspondences were of size  $K \times K$ , with  $K = 50$ , and using a spectral upsampling step of  $k_{\text{step}} = 5$ , these maps were refined until dimension 100 was reached. The refined network then provided correspondences between any two shapes in the collection, even if the two shapes were not directly connected by an edge inside the network. These correspondences were of high quality and significantly improved those obtained by simple ICP alignment, and were then used for our subsequent morphometric analysis.

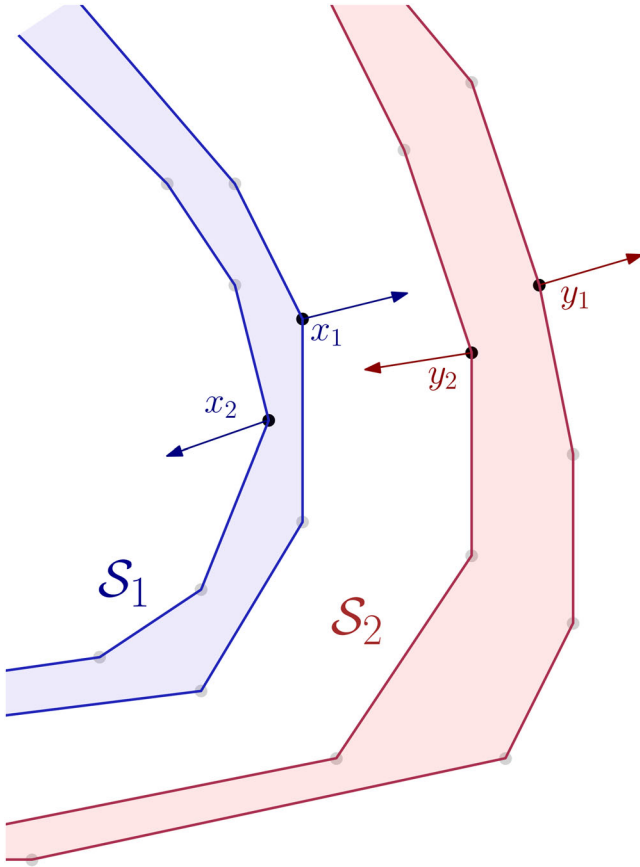


**FIGURE 5** Local significance of the normal consistency scheme for inner and outer surfaces.

## 2.5 | Deformation analysis

### 2.5.1 | Unsupervised analysis

As we sought to perform template-based morphometric analysis but only had access to a “limit shape” (Huang et al., 2019) that did not correspond to any known geometry, we designed a method to extract an actual shape from the collection that was the most intrinsically similar to the limit shape. We defined the intrinsic dissimilarity between shape  $i$  and the limit shape as  $\|D_c^{(i)} - I\|_{H_b^2}^2$  where  $D_c^{(i)}$  was the conformal characteristic shape difference (Huang et al., 2019; Rustamov et al., 2013), a  $K \times K$  matrix which captures the differences between the limit shape and shape  $i$ ,  $I$  was the identity matrix, and  $\|\cdot\|_{H_b^2}^2$  the norm in the Sobolev space (Rustamov et al., 2013). The shape that minimized this dissimilarity metric was called  $T$ , and can be conceived as a median shape of the collection. Note that correspondences between  $T$  and each shape in the collection were then available thanks to the FMN, mentioned above.

Using shape  $T$ , acting as a template, we generated for each shape  $S_i$  a vertex-wise deformation field  $d^{(i)}$  deforming  $T$  into  $S_i$ . This deformation was defined by first rigidly aligning the two shapes using

the computed correspondences and then using the vertex-wise displacement in 3D provided by the same correspondences. We further smoothed the deformation fields following the approach from (Eisenberger, Lahner, & Cremers, 2020; Eisenberger, Toker, et al., 2020), projecting  $d^{(i)}$  into the truncated Laplacian basis using  $K_d$  eigenvectors, with  $K_d = 100$ .

Using deformation fields as embeddings for shapes, we performed a principal component analysis (PCA) to extract principal components  $(D_j)_{j=1}^{p_{pca}}$ , which we here called principal deformations. Note that projecting the deformation fields into these components provided a new reduced embedding  $\tilde{d}^{(i)} \in \mathbb{R}^{p_{pca}}$  for each shape  $S_i$ . Principal deformations can be thought of as deformations of the template  $T$  to  $\mathbb{R}^3$ , and could be visualized by applying deformation  $tD_j$  to the template  $T$  for various values of  $t \in \mathbb{R}$ . Note that we informally referred to as a positive (resp. negative) deformation the visualization of  $tD_j$  with  $t > 0$  (resp.  $t < 0$ ). This visualization provided a qualitative feedback in addition to the standard projection on the first components.

### 2.5.2 | Supervised analysis

The procedure up to the current point was fully unsupervised in the sense that no manual intervention or labels were used. To validate the previous analysis, we trained a logistic regression model to predict to which group a skull belonged, using only  $(\tilde{d}^{(i)})_{i=1}^N$  as input. This step demonstrated that the fully unsupervised analysis generated a meaningful representation for each shape. For each class, the logistic regression learned a vector  $\beta$  so that a high value of  $\langle \tilde{d}^{(i)}, \beta \rangle_2$  meant that  $\tilde{d}^{(i)}$  was predicted to belong to the given class. For visualization purposes, we built the reference deformation  $D(\beta) = \sum_{j=1}^{p_{pca}} \beta_j D_j$  which corresponded to the “canonical” deformation of the template associated with the given class. That is, deformations of the template which aligned the most with  $D(\beta)$  were predicted to be part of the given class, and thus the deformation  $D(\beta)$  provided a visual representation of how the classification decision for each class is made.

We performed a PCA and computed logistic regression models using the first  $p_{pca} = 10$  components. We fitted five types of logistic regressions: (1) trigonocephaly versus controls (C-T), (2) (controls + metopic ridges) versus trigonocephaly ([C + M]-T), (3) controls versus metopic ridges versus trigonocephaly (C-M-T), and (4) metopic ridges versus trigonocephaly (M-T) (5) metopic ridges versus controls (C-M). We evaluate these regressions using a fivefold cross validation, weighting samples to compensate for the nonuniform distribution of labels.

We compared our results to another fully unsupervised baseline, by applying a similar logistic regression to the standard Shape-DNA descriptor (Reuter et al., 2009). This global shape descriptor embeds the shape as the list of the first  $K_{dna}$  normalized eigenvalue of its Laplace-Beltrami operator. We tested several values of  $K_{dna}$ , and obtained best results using 100 eigenvalues.

### 3 | RESULTS

#### 3.1 | FMN

The refined networks allowed us to obtain per-vertex correspondences between any pair of shapes (Figure 6) within the collection, which improved upon those obtained by the initial ICP alignment. In Figure 6, we visualized the computed point-to-point correspondences. Specifically, we first associated color (r, g, b) values based on the (x, y, z) coordinates of each point on the leftmost shape. We then transferred these color values using the computed correspondences onto the rightmost shape. Thus, points with same (r, g, b) values are seen as corresponding. Note the overall smoothness of the

transferred colors. This was a nontrivial task, and obtaining visually satisfying correspondences was a necessary condition for quality.

#### 3.2 | Extrinsic analysis

##### 3.2.1 | Unsupervised analysis

To perform our analysis, we first extracted the implicit template  $T$  (Figure 7, top), which can be deformed smoothly into any shape in the collection using the network (Figure 8). Finally, adding the average deformation to the template allowed the correction of its geometry (Figure 7, bottom). This correction step was performed for

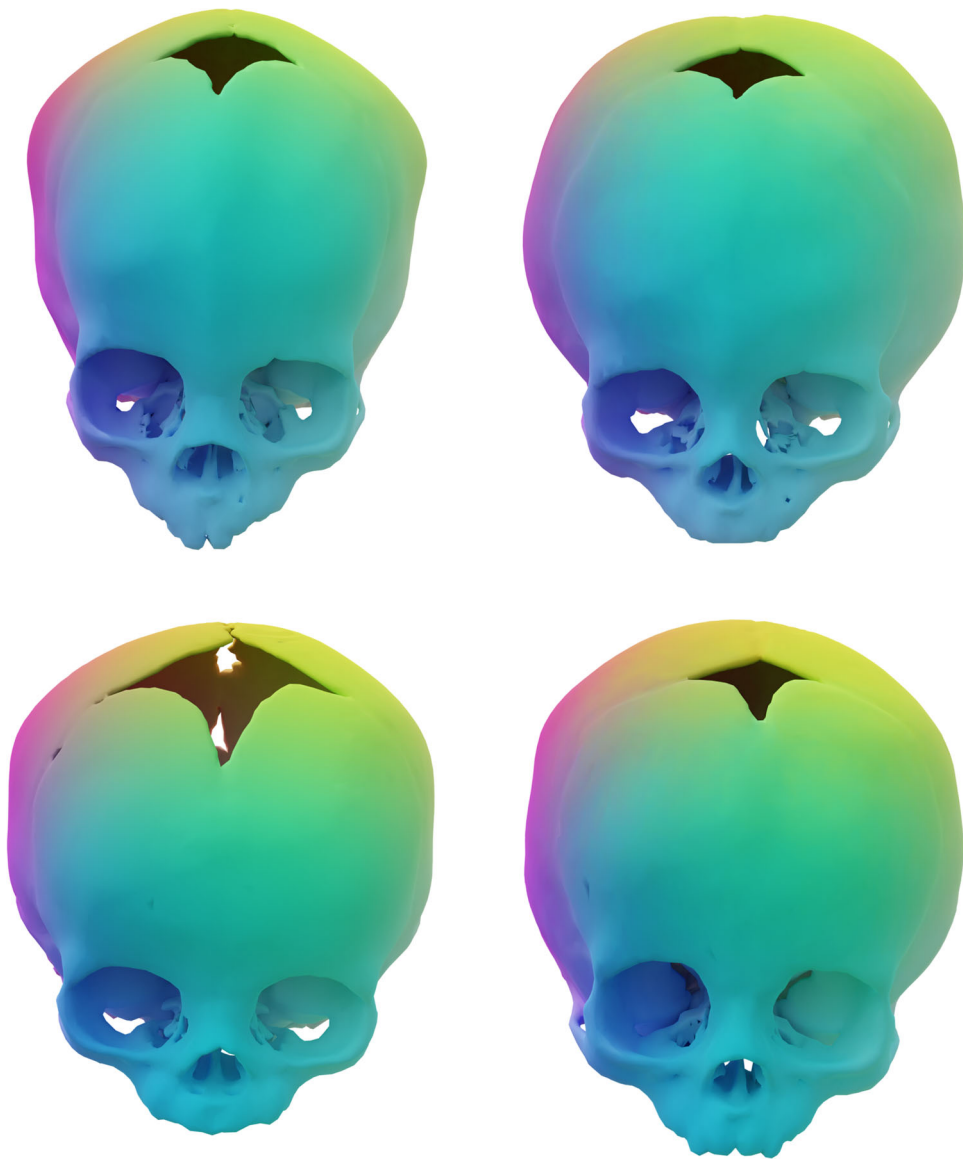


**FIGURE 6** Visualization of computed correspondences between two random pairs of shapes in the collection. Top: correspondence between two nearly isometric scans. bottom: correspondences between highly nonisometric scans. Vertices on the left are given RGB colors depending on their XYZ coordinates, and corresponding vertices between left and right are given the same color.

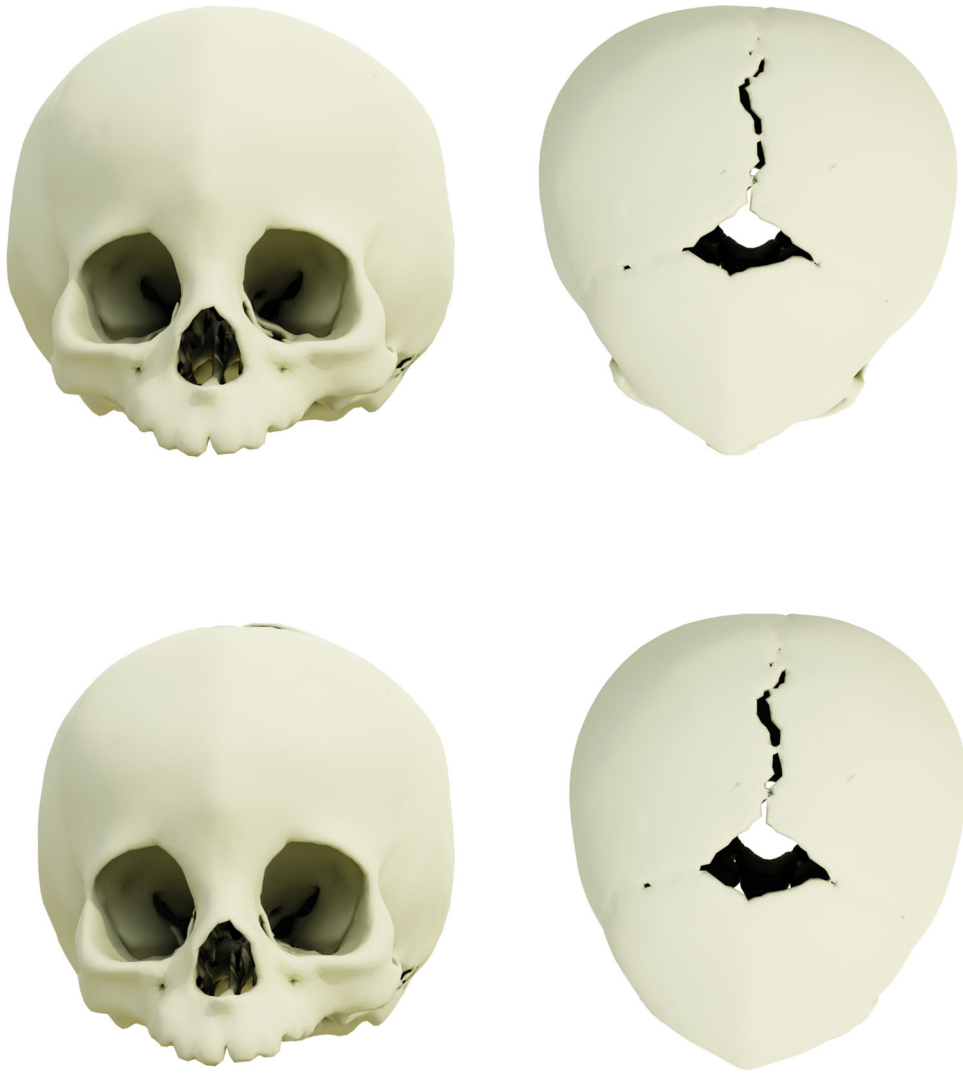


**FIGURE 7** Top: Surrogate template chosen as the closest to the limit shape. Bottom: Corrected template by applying the average deformation to the template.

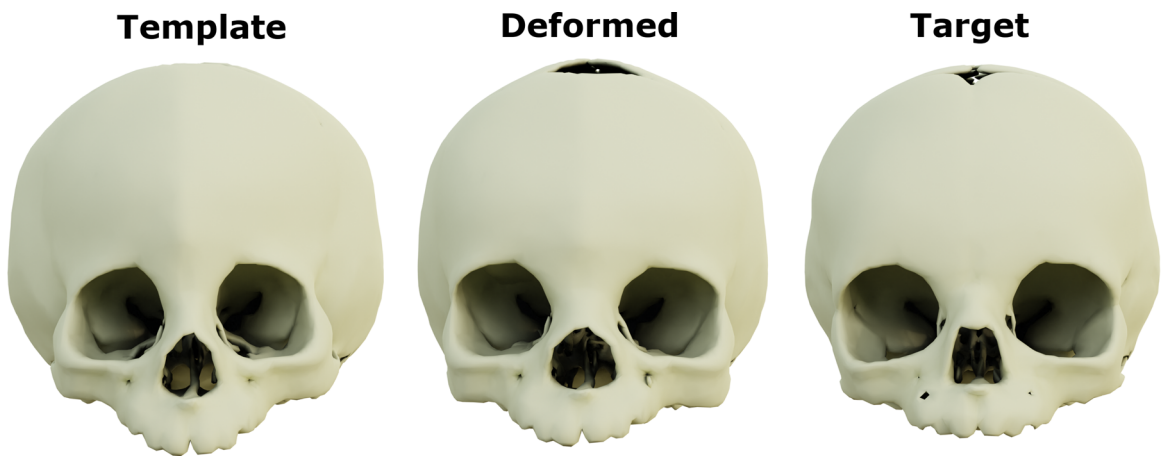


**FIGURE 8** Example of the computed deformation between the template and a shape from the data set.

**TABLE 1** Average true positive rates (TPR) after cross-validation for multiple logistic regression objectives, differentiating control against trigonocephaly (C-T), control and metopic crests together against trigonocephaly ([C + M]-T), and eventually control against metopic crests against trigonocephaly (C-MT).

Methods	C-T	(C + M)-T	C-M-T	M-T	C-M
Shape-DNA	66.0%	64.4%	46.5%	69.2%	53.3%
Ours	92.9%	91.1%	76.4%	85.3%	72.2%

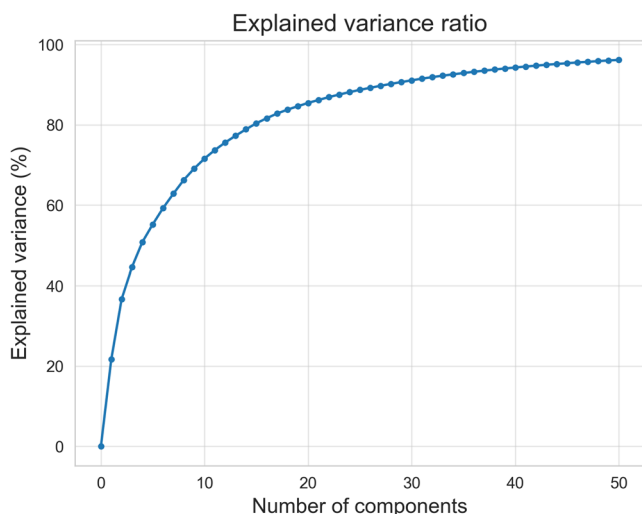


**FIGURE 9** Cumulative explained variance ratio of the PCA. PCA, principal component analysis.

visualization purposes only, as the PCA used in our quantitative analysis automatically factored this average deformation out.

### 3.2.2 | Logistic regressions

We provide average true positive rates (TPR) of the five types of logistic regressions on the validation set in Table 1. For comparison, we added results of performing similar regressions using the standard Shape-DNA descriptor (Reuter et al., 2009) as input.

The principal components of the PCA carried deformations of the template and were referred to as principal deformations (Section 2.5). The cumulative variances explained by the principal components were displayed in Figure 9, while Figure 10 showed the projection of the data set on the fourth and seventh components, which displayed more separation than the first two. The theoretical deformation associated with the positive and negative values of each of the first two principal components were displayed in Figure 11. As explained in Section 2.5, the logistic regression learned for each class a representative deformation of the template to classify each skull which enables us to generate a “typical” skull for each cohort, built by exaggerating the representative deformation. In Figure 12, we displayed such “typical” skulls for each class next to the template.

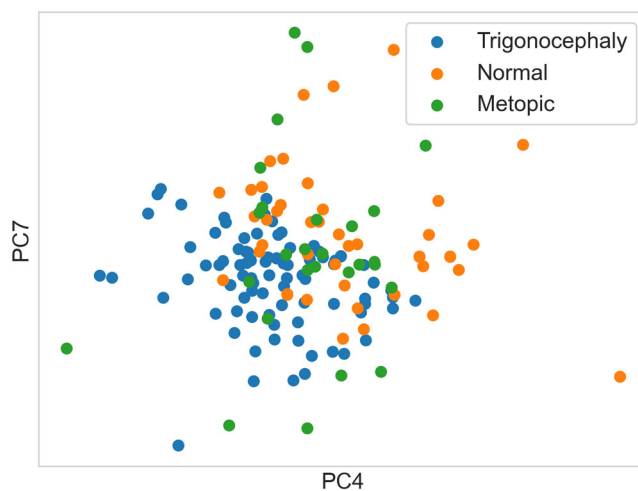


**FIGURE 10** Projection of the data set on the fourth and seventh principal components.

### 3.2.3 | Computational efficiency

After preprocessing, refining the FMN made of 155 scans took 40 min, the main bottleneck lying in the eigendecomposition of a large sparse matrix. Note that this can be improved by reducing the number of provided initial correspondences. The downstream analysis takes a few minutes to compute.

## 4 | DISCUSSION

We showed (Table 1) that a landmark-free approach, based on state-of-the-art spectral analysis tools, can reliably distinguish trigonocephaly from normal skulls and skulls with metopic ridges. The specific diagnosis of metopic ridges was not straightforward, especially compared to the control cohort, but the clinical relevance of our results consisted in the fact that ridges were separated from trigonocephaly, which is the main practical issue when managing patients with “triangular foreheads.” In contrast, the Shape-DNA based approach failed to make reliable predictions on the validation set. This is because the distinctions between different classes (and, in particular trigonocephaly and metopic ridges) pertains to local geometrical characteristics. Thus, a method, based on a global shape descriptor, such as the Shape-DNA, is unable to reliably extract the signal necessary for such a distinction. We identified two primary factors contributing to incorrect classification in our experimental setup. First, cases where the surfaces exhibited significant issues, such as substantial missing or additional parts, were found to lead to misclassification (Figure 13). Second, incorrect correspondences between surfaces resulted in outliers in the deformations, and this issue was observed to be influenced by mesh quality, particularly in the orbital cavity region.

We also showed that our method could produce a clear representation of the classification outcomes (Figure 12). Notably, we observed that trigonocephaly was detected when associated to pronounced

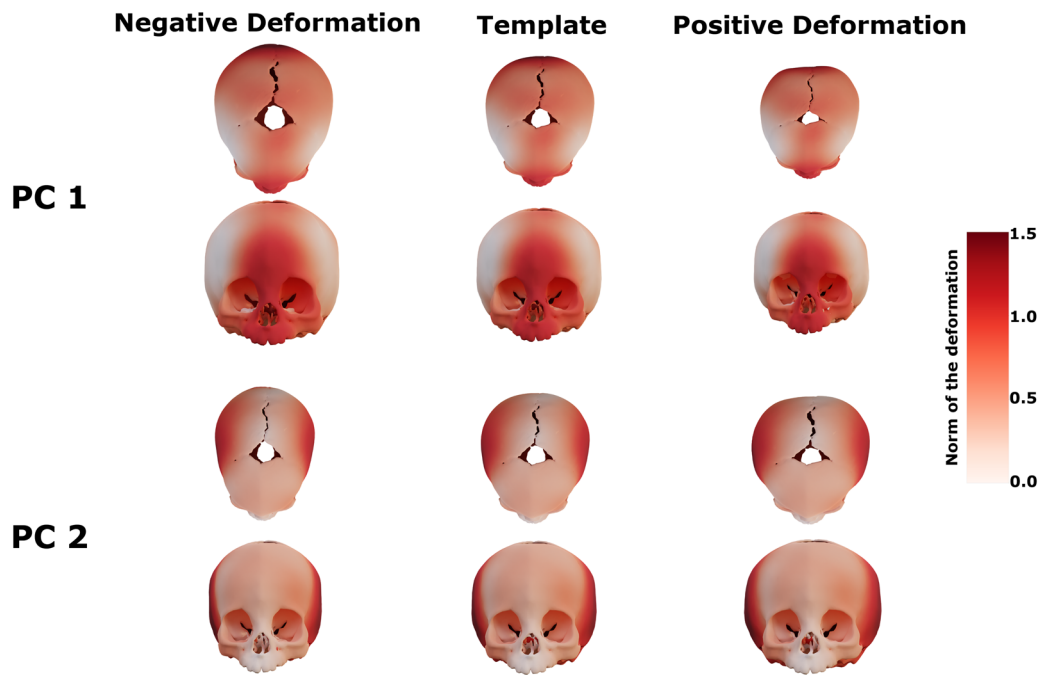


**FIGURE 11** Visualization of the first principal deformations  $D_j$  for  $j = 1, 2$ . For each component the leftmost and rightmost shapes displayed the two opposite deformations. The color indicated the norm of the displacement  $D_j$  at each vertex.

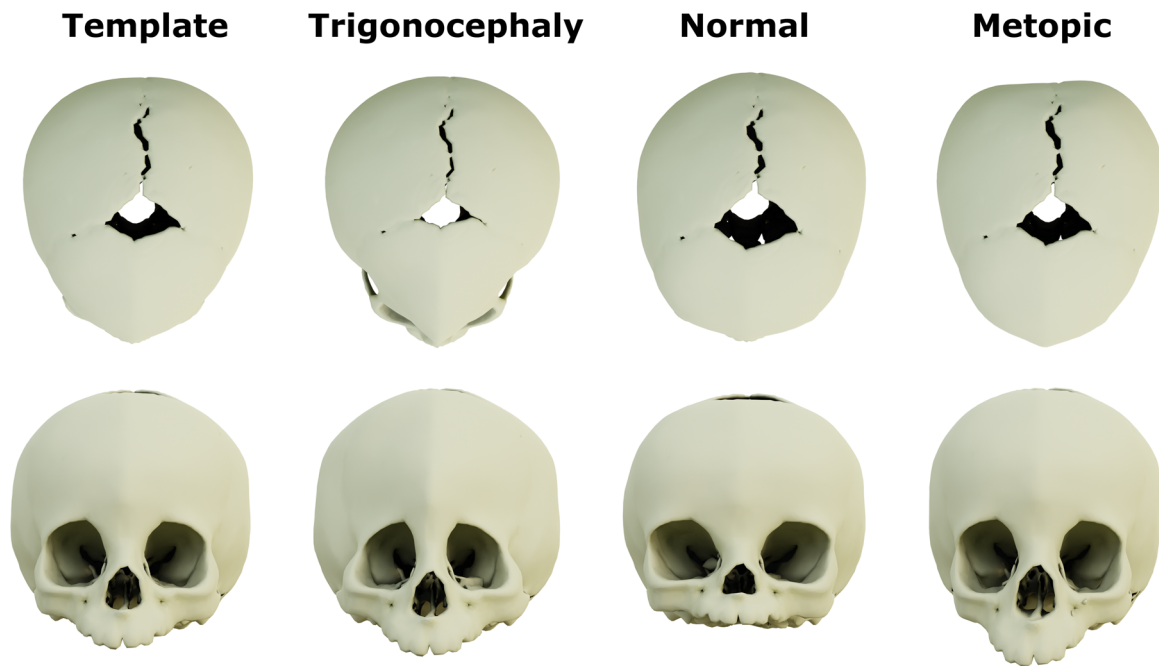


**FIGURE 12** “Typical” skull for each class, as detected by the logistic regression. The deformation was exaggerated for visualization purposes. Note that these skulls don’t represent actual patient but the deformations on which each embedding is projected.

deformations in both the forehead and the orbit regions. In contrast, the deformation associated with metopic ridges lied between the one for the control group and for the trigonocephaly group, with a relatively minimal impact on orbital morphology, consistent with expectations from usual clinical observations. Nevertheless, it is important to be cautious when analyzing such visualizations, as they only indicated the overall direction in

which each deformation was projected. Indeed, following Figure 12, the model seemed to heavily rely on age as a distinguishing factor. However, we demonstrated in the supplementary material that this feature did not offer a reliable signal.

We also highlight that our method directly ran on raw surfaces without specific manual processing such as closing holes or

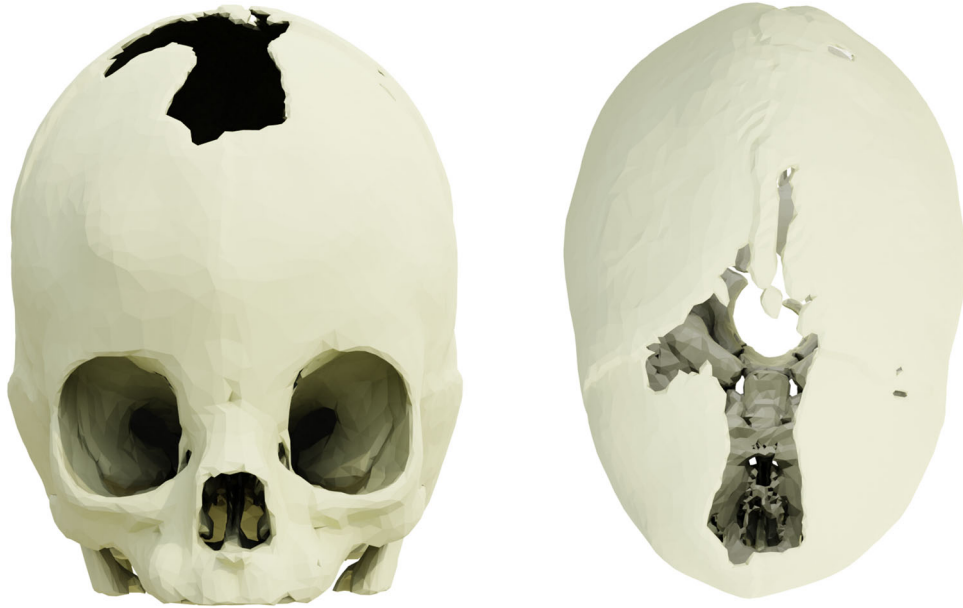


**FIGURE 13** Example of misclassification due to a large missing part. This patient was predicted to be a normal skull while it belongs to the metopic group.

smoothing, and did not require any manual intervention such as annotated regions or landmarks. While this results in several challenges for many approaches, the efficiency of our method in this scenario hints at its potential generality. These lower requirements, associated to a rather simple underlying statistical model justified that the TPR for our classifications were lower than similar works using this additional information.

While spectral methods have already been applied to biomedical data (Kitchell et al., 2018; Klein et al., 2017; Melzi et al., 2016; Niethammer et al., 2007; Nitzken et al., 2014; Shishegar et al., 2021), the pipeline proposed here is the first attempt to leverage the recent functional maps-based methods for fully automatic dense point-to-point correspondence computation, to a clinical question. Landmark-free approaches in general are highly relevant in morphometrics, especially in a clinical context where simple and objective tools have to be provided to medical practitioners. Spectral approaches seem promising in designing shape-based diagnostic tools for craniofacial surgeons, with the possibility to easily extend the data set without major computational costs and to include multiple diagnostic categories as illustrated here. Regarding the diagnosis of trigonocephaly, methods based on 3D data proposed in the literature are still scarce (Bhalodia et al., 2020; Bloch et al. n.d.; Schaufelberger et al., 2022), and spectral approaches could be an interesting alternative for designing diagnostic tools, assessing growth in temporal series, and for evaluating results of medical or surgical treatments.

More broadly, this pipeline also appears interesting as it provides a general framework bringing together functional maps and morphometrics. It leverages first the flexibility and generality of spectral methods, allowing to work at high calculation speeds

and processing entire collections efficiently, on data sets involving a great variety of shapes undergoing potentially major deformations. Our approach furthermore offers clear visual feedback of the results, highlighting the main zones of deformations across cohorts and enabling direct classification of diagnostic, overcoming the burden of designing a template or manually specifying landmarks or keypoints. Finally, as minimal information about skulls themselves was used, namely the rough pre-alignment and the normal consistency scheme, the complete pipeline can easily be adapted to new collections of shapes with little adjustment.

## 5 | CONCLUSION

In this work, we applied recent spectral shape matching developments to the detection of trigonocephaly in young children. Our method is fully automatic, and especially does not require manual placement on landmarks on CT scans, and can be generalized to other diseases. Results clearly outperform standard spectral methods as they detect local deformations of the skulls, which motivates the use of such new methods to morphometric analysis.

**Algorithm 1.** General pipeline for our algorithm

- 
- Require:** Input: Collection of shapes
- 1: Compute initial correspondences (Section 2.4)
  - 2: Refine correspondences (Section 2.4)
  - 3: Extract a template and deformations (Section 2.5)
  - 4: Perform deformation analysis (Section 2.5)
-

## AUTHOR CONTRIBUTIONS

**Robin Magnet:** Writing—original draft; methodology; visualization; investigation; conceptualization; validation; formal analysis; writing—review and editing. **Kevin Bloch:** Conceptualization; validation; data curation; writing—review and editing; methodology; writing—original draft. **Maxime Taverne:** Conceptualization; writing—review and editing; formal analysis; methodology. **Simone Melzi:** Conceptualization; project administration; writing—review and editing; methodology. **Maya Geoffroy:** Methodology; Writing—review and editing. **Roman H. Khonsari:** Methodology; validation; project administration; writing—review and editing; writing—original draft; conceptualization; supervision. **Maks Ovsjanikov:** Supervision; project administration; resources; writing—review and editing; writing—original draft.

## ACKNOWLEDGMENTS

We acknowledge Dr. Giovanna Paternoster, Dr. Eric Arnaud and Dr. Syril James (craniofacial surgeons), Jean Feydi (theoretical morphometrics), Pr. Nathalie Boddart (medical imaging), Pr. Sébastien Laporte and Pr. Mehran Moazen (biomechanics), Dr. Lara van de Lande (maxillofacial surgery) for their valuable help. Parts of this work were supported by the ERC Starting Grant No. 758800 (EXPROTEA) and the ANR AI Chair AIGRETTE.

## DATA AVAILABILITY STATEMENT

The data that support the findings of this study are available on request from the corresponding author. The data are not publicly available due to privacy or ethical restrictions.

## PEER REVIEW

The peer review history for this article is available at <https://www.webofscience.com/api/gateway/wos/peer-review/10.1002/jmor.21609>.

## ORCID

Robin Magnet  <http://orcid.org/0000-0002-2192-411X>

Maxime Taverne  <http://orcid.org/0000-0003-3355-6200>

Roman H. Khonsari  <https://orcid.org/0000-0002-0649-1432>

Maks Ovsjanikov  <https://orcid.org/0000-0002-5867-4046>

## REFERENCES

- Adams, D. C., Rohlf, F. J., & Slice, D. E. (2004). Geometric morphometrics: Ten years of progress following the 'revolution'. *Italian Journal of Zoology*, 71(1), 5–16.
- Arnqvist, G., & Mårtensson, T. (1998). Measurement error in geometric morphometrics: Empirical strategies to assess and reduce its impact on measures of shape. *Acta Zoologica Academiae Scientiarum Hungaricae*, 44, 73–96.
- Attai, S., Pai, G., & Ovsjanikov, M. (2021). "DPFM: Deep partial functional maps". In: *2021 International Conference on 3D Vision (3DV)*. IEEE, pp. 175–185.
- Besl, P. J., & McKay, N. D. (1992). Sensor fusion IV: Control paradigms and data structures, *Method for registration of 3-D shapes* (Vol. 1611, pp. 586–606). Spie.
- Bhalodia, R., Dvoracek, L. A., Ayyash, A. M., Kavan, C., Whitaker, R., & Goldstein, J. A. (2020). Quantifying the severity of metopic craniosynostosis: A pilot study application of machine learning in craniofacial surgery. *Journal of Craniofacial Surgery*, 31(3), 697–701.
- Biasotti, S., Cerri, A., Bronstein, A., & Bronstein, N. (2016). Recent trends, applications, and perspectives in 3D shape similarity assessment. *Computer Graphics Forum*, 35(6), 87–119.
- Birgfeld, C. B., Heike, C. L., Al-Mufarrej, F., Oppenheimer, A., & Kamps, S. E. (2019). Practical computed tomography scan findings for distinguishing metopic craniosynostosis from metopic ridging. *Plastic and Reconstructive Surgery. Global Open*, 7(3):e1944.
- Birgfeld, C. B., Saltzman, B. S., Hing, A. V., Heike, C. L., Khanna, P. C., Gruss, J. S., & Hopper, R. A. (2013). Making the diagnosis: Metopic ridge versus metopic craniosynostosis. *The Journal of Craniofacial Surgery*, 24(1), 178–185.
- Bloch, K. (n.d.). "New diagnostic criteria for metopic ridges and trigonocephaly: A 3D geometric approach." Submitted in *Plastic and Reconstructed Surgery*.
- Bookstein, F. L. (1982). Foundations of morphometrics. *Annual Review of Ecology and Systematics*, 13(1), 451–470.
- Bookstein, F. L. (1997). *Morphometric tools for landmark data*.
- Bookstein, F. L. (2019). Pathologies of between groups principal components analysis in geometric morphometrics. *Evolutionary Biology*, 46(4), 271–302.
- Calandrelli, R., Pilato, F., Massimi, L., Marrazzo, A., Panfili, M., Di Rocco, C., & Colosimo, C. (2020). Orbito-facial dysmorphism in patients with different degrees of trigonocephaly severity: Quantitative morpho-volumetric analysis in infants with non-syndromic metopic craniosynostosis. *Child's Nervous System: ChNS: Official Journal of the International Society for Pediatric Neurosurgery*, 36(6), 1263–1273.
- Cho, M.-J., Kane, A. A., Seaward, J. R., & Hallac, R. R. (2016). Metopic "ridge" vs. "craniosynostosis": Quantifying severity with 3D curvature analysis. *Journal of Cranio-Maxillo-Facial Surgery: Official Publication of the European Association for Cranio-Maxillo-Facial Surgery*, 44(9), 1259–1265.
- von Cramon-Taubadel, N., Frazier, B. C., & Lahr, M. M. (2007). The problem of assessing landmark error in geometric morphometrics: Theory, methods, and modifications. *American Journal of Physical Anthropology*, 134(1), 24–35.
- Daboul, A., Ivanovska, T., Bülow, R., Biffar, R., & Cardini, A. (2018). Procrustes-based geometric morphometrics on MRI images: An example of inter-operator bias in 3D landmarks and its impact on big datasets. *PLOS One*, 13(5):e0197675.
- Dyke, R. M., Lai, Y.-K., Rosin, P. L., Zappalà, S., Dykes, S., Guo, D., Li, K., Marin, R., Melzi, S., & Yang, J. (2020). SHREC'20: Shape correspondence with non-isometric deformations. *Computers & Graphics*, 92, 28–43.
- Eisenberger, M., Lahner, Z., & Cremers, D. (2020). "Smooth shells: Multi-scale shape registration with functional maps". In: *Proceedings of the IEEE/CVF Conference on Computer Vision and Pattern Recognition*, pp. 12265–12274.
- Eisenberger, M., Toker, A., Leal-Taixé, L., & Cremers, D. (2020). "Deep shells: Unsupervised shape correspondence with optimal transport". In: *Advances in Neural Information Processing Systems* 33.
- Fabre, A.-C., Bardua, C., Bon, M., Clavel, J., Felice, R. N., Streicher, J. W., Bonnel, J., Stanley, E. L., Blackburn, D. C., & Goswami, A. (2020). Metamorphosis shapes cranial diversity and rate of evolution in salamanders. *Nature Ecology & Evolution*, 4(8), 1129–1140.
- Fedorov, A., Beichel, R., Kalpathy-Cramer, J., Finet, J., Fillion-Robin, J. C., Pujol, S., Bauer, C., Jennings, D., Fennessy, F., Sonka, M., Buatti, J., Aylward, S., Miller, J. V., Pieper, S., & Kikinis, R. (2012). 3D Slicer as an image computing platform for the Quantitative Imaging Network. *Magnetic Resonance Imaging*, 30(9), 1323–1341.

- Gillet, A., Frédérick, B., & Parmentier, E. (2019). Divergent evolutionary morphology of the axial skeleton as a potential key innovation in modern cetaceans. *Proceedings of the Royal Society B: Biological Sciences*, 286(1916):20191771.
- Gunz, P., & Mitteroecker, P. (2013). Semilandmarks: a method for quantifying curves and surfaces. *Hystrix, the Italian Journal of Mammalogy*, 24(1), 103–109.
- Huang, R., Achlioptas, P., Guibas, L., & Ovsjanikov, M. (2019). Limit shapes—A tool for understanding shape differences and variability in 3D model collections. *Computer Graphics Forum*, 38(5), 187–202.
- Huang, R., Ren, J., Wonka, P., & Ovsjanikov, M. (2020). Consistent ZoomOut: Efficient spectral map synchronization. *Computer Graphics Forum*, 39(5), 265–278.
- Kellogg, R., Allori, A. C., Rogers, G. F., & Marcus, J. R. (2012). Interfrontal angle for characterization of trigonocephaly: Part 1: Development and validation of a tool for diagnosis of metopic synostosis. *The Journal of Craniofacial Surgery*, 23(3), 799–804.
- Kitchell, L., Bullock, D., Hayashi, S., & Pestilli, F. (2018). Shape analysis of white matter tracts via the Laplace-Beltrami spectrum. *Shape in Medical Imaging*, 11167, 195–206.
- Klein, A., Ghosh, S. S., Bao, F. S., Giard, J., Häme, Y., Stavsky, E., Lee, N., Rossa, B., Reuter, M., Neto, E. C., & Keshavan, A. (2017). Mindboggling morphometry of human brains. *PLOS Computational Biology*, 13(2), e1005350.
- Klingenberg, C. P. (2002). Morphometrics and the role of the phenotype in studies of the evolution of developmental mechanisms. *Gene*, 287(1–2), 3–10.
- Klingenberg, C. P. (2016). Size, shape, and form: Concepts of allometry in geometric morphometrics. *Development Genes and Evolution*, 226(3), 113–137.
- Kolar, J. C., & Salter, E. M. (1997). Preoperative anthropometric dysmorphology in metopic synostosis. *American Journal of Physical Anthropology*, 103(3), 341–351.
- Mallet, C., Cornette, R., Billet, G., & Houssaye, A. (2019). Interspecific variation in the limb long bones among modern rhinoceroses—Extent and drivers. *PeerJ*, 7, e7647.
- Mathijssen, I. M. J., Working Group Guideline Craniosynostosis. (2021). Updated guideline on treatment and management of craniosynostosis. *The Journal of Craniofacial Surgery*, 32(1), 371–450.
- Melzi, S., Mella, A., Squarcina, L., Bellani, M., Perlini, C., Ruggeri, M., Altamura, C. A., Brambilla, P., & Castellani, U. (2016). Functional maps for brain classification on spectral domain. In M. Reuter, C. Wachinger, & H. Lombaert (Eds.), *Spectral and shape analysis in medical imaging* (pp. 25–35). Springer International Publishing.
- Melzi, S., Mella, A., Squarcina, L., Bellani, M., Perlini, C., Ruggeri, M., Altamura, C. A., Brambilla, P., & Castellani, U. (2019). ZoomOut: Spectral upsampling for efficient shape correspondence. *ACM Transactions on Graphics*, 155, 1–14.
- van der Meulen, J., van der Hulst, R., van Adrichem, L., Arnaud, E., Chin-Shong, D., Duncan, C., Habets, E., Hinojosa, J., Mathijssen, I., May, P., Morrirt, D., Nishikawa, H., Noons, P., Richardson, D., Wall, S., van der Vlugt, J., & Renier, D. (2009). The increase of metopic synostosis: A pan-European observation. *The Journal of Craniofacial Surgery*, 20(2), 283–286.
- Nguyen, A., Ben-Chen, M., Welnicka, K., Ye, Y., & Guibas, L. (2011). An optimization approach to improving collections of shape maps. *Computer Graphics Forum*, 30(5), 1481–1491.
- Niethammer, M., Reuter, M., Wolter, F.-E., Bouix, S., Peinecke, N., Koo, M.-S., & Shenton, M.E. (2007). Global medical shape analysis using the Laplace-Beltrami spectrum. In N. Ayache, S. Ourselin, & A. Maeder (Eds.), *Medical image computing and computer-assisted intervention—MICCAI 2007* (Vol. 4791, pp. 850–857).
- Nitzken, M. J., Casanova, M. F., Gimelfarb, G., Inanc, T., Zurada, J. M., & El-Baz, A. (2014). Shape analysis of human brain: A brief survey. *IEEE Journal of Biomedical and Health Informatics*, 18(4), 1337–1354.
- O'Higgins, P., & Jones, N. (1998). Facial growth in *Cercopithecus torquatus*: An Application of threedimensional geometric morphometric techniques to the study of morphological variation. *Journal of Anatomy*, 193(Pt 2), 251–272.
- Ovsjanikov, M., Ben-Chen, M., Solomon, J., Butscher, A., & Guibas, L. (2012). Functional maps: A flexible representation of maps between shapes. *ACM Transactions on Graphics (TOG)*, 31(4), 1–11.
- Ovsjanikov, M., Corman, E., Bronstein, M., Rodolà, E., Ben-Chen, M., Guibas, L., Chazal, F., & Bronstein, A. (2017). Computing and processing correspondences with functional maps. In *ACM GRAPH 2017 Courses (SIGGRAPH '17)* (pp. 1–62).
- Palci, A., & Lee, M. S. Y. (2019). Geometric morphometrics, homology and cladistics: Review and recommendations. *Cladistics*, 35(2), 230–242.
- Ren, J., Melzi, S., Wonka, P., & Ovsjanikov, M. (2021). Discrete optimization for shape matching. *Computer Graphics Forum*, 40(5), 81–96.
- Ren, J., Poulencard, A., Wonka, P., & Ovsjanikov, M. (2018). Continuous and orientation-preserving correspondences via functional maps. *ACM Transactions on Graphics (ToG)*, 37(6), 1–16.
- Reuter, M., Wolter, F.-E., Shenton, M.E., & Niethammer, M. (2009). Laplace-Beltrami eigenvalues and topological features of eigenfunctions for statistical shape analysis. *Computer Aided Design*, 41(10), 739–755.
- Rodolà, E., Cosmo, L., Bronstein, M., Torsello, A., & CremersHide, D. (2017). Partial functional correspondence. *Computer Graphics Forum*, 36(1), 222–236.
- Rustamov, R. M., Ovsjanikov, M., Azencot, O., Ben-Chen, M., Chazal, F., & Guibas, L. J. (2013). Map-based exploration of intrinsic shape differences and variability. *ACM Transactions on Graphics*, 32(4), 1.
- Rutland, J. W., Bellaire, C. P., Yao, A., Arrighi-Allisan, A., Napoli, J. G., Delman, B. N., & Taub, P. J. (2021). The expanding role of geometric morphometrics in craniofacial surgery. *Journal of Craniofacial Surgery*, 32(3), 1104–1109.
- Sahillioğlu, Y. (2020). Recent advances in shape correspondence. *The Visual Computer*, 36(8), 1705–1721.
- Schafelberger, M., Kühle, R., Wachter, A., Weichel, F., Hagen, N., Ringwald, F., Eisenmann, U., Hoffmann, J., Engel, M., Freudlsperger, C., & Nahm, W. (2022). A radiation-free classification pipeline for craniosynostosis using statistical shape modeling. *Diagnostics*, 12(7), 1516.
- Shishegar, R., Pizzagalli, F., Georgiou-Karistianis, N., Egan, G. F., Jahanshad, N., & Johnston, L. A. (2021). A gyrification analysis approach based on Laplace Beltrami eigenfunction level sets. *Neuroimage*, 229, 117751.
- Slice, D. E. (2007). Geometric morphometrics. *Annual Review of Anthropology*, 36, 261–281.
- Toussaint, N., Redhead, Y., Vidal-García, M., Vercio, L. L., Liu, W., Fisher, E. M. C., Hallgrímsson, B., Tybulewicz, V. L. J., Schnabel, J. A., & Green, J. B. A. (2021). A landmark-free morphometrics pipeline for high-resolution phenotyping: Application to a mouse model of Down syndrome. *Development*, 148, 18.
- Wärmländer, S. K. T. S., Garvin, H., Guyomarc'h, P., Petaros, A., & Sholts, S. B. (2019). Landmark typology in applied morphometrics studies: What's the point. *The Anatomical Record*, 302(7), 1144–1153.
- Watanabe, A., & Slice, D. E. (2014). The utility of cranial ontogeny for phylogenetic inference: A case study in crocodylians using geometric morphometrics. *Journal of Evolutionary Biology*, 27(6), 1078–1092.

Webster, M. A. R. K., & Sheets, H. D. (2010). A practical introduction to landmark-based geometric morphometrics. *The Paleontological Society Papers*, 16, 163–188.

### **SUPPORTING INFORMATION**

Additional supporting information can be found online in the Supporting Information section at the end of this article.

**How to cite this article:** Magnet, R., Bloch, K., Taverne, M., Melzi, S., Geoffroy, M., Khonsari, R. H., & Ovsjanikov, M. (2023). Assessing craniofacial growth and form without landmarks: A new automatic approach based on spectral methods. *Journal of Morphology*, 284, e21609. <https://doi.org/10.1002/jmor.21609>